Supporting Information for

Graphene-Based Single-Atom Catalysts for Electrochemical CO_2 Reduction: Unraveling the Roles of Metals and Dopants in Tuning Activity

Colin Gallagher, Manish Kothakonda, and Qing Zhao*

Department of Chemical Engineering, Northeastern University, Boston, Massachusetts, 02115, United States

Contents

Supplementary Method. SAC optimization. We developed a systematic approach to locate the most stable configuration of both the clean and CO-adsorbed SAC structures.

Case I. For each clean SAC, we started from a planar geometry and performed full geometry optimization with both atomic positions and lattice parameters relaxed (ISIF = 3) using conjugate gradient algorithm (IBRION = 2). We then built the initial geometry of CO-adsorbed SAC based on the optimized clean SAC structure and performed a subsequent geometry optimization with only atomic positions relaxed (ISIF = 2). However, we observed that the CO-adsorbed structure occasionally converged to a CO-desorbed geometry with relatively high energy using conjugate gradient algorithm, while converged to a more reasonable geometry with CO still adsorbed on the surface and with relatively low energy using quasi-Newton algorithm (IBRION = 1). In this situation, we used the structure and energy optimized using quasi-Newton algorithm to calculate CO adsorption energy.

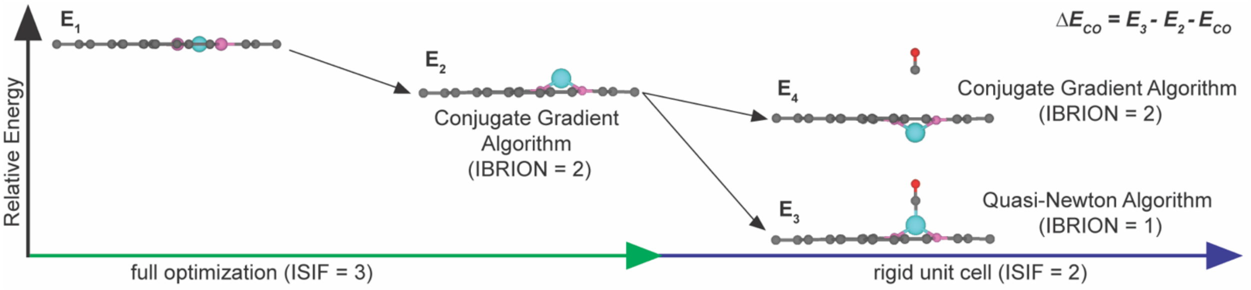

Case II. In some cases, the planar geometry of clean SAC was preserved in geometry optimization. However, a local out-of-plane distortion around the active site was observed after CO is adsorbed on the surface. We removed the CO adsorbate and reoptimized the clean surface with out-of-plane distortion using quasi-Newton algorithm and obtained an optimized clean surface with lower energy than the optimized planar structure. In this situation, we used the clean SAC with out-of-plane distortion and lower energy in CO adsorption energy calculation.

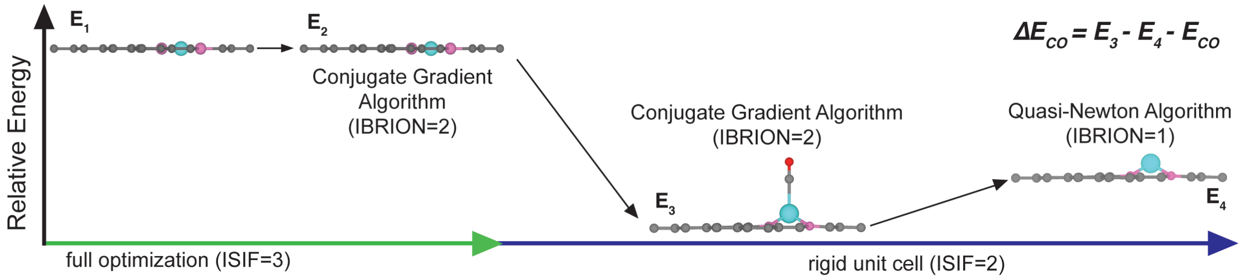

Case III. In the least frequent scenario, the planar structure of clean SAC was preserved in initial geometry optimization. However, CO adsorbate desorbed from SAC in the subsequent geometry optimization. We then removed the CO adsorbate and reoptimized the SAC with out-of-plane distortion using quasi-Newton algorithm and obtained an optimized clean surface with lower energy than the optimized planar structure. We then reintroduced the CO adsorbate and performed a subsequent geometry optimization using quasi-Newton algorithm and obtained a more stable geometry with CO adsorbed on the surface than the desorption configuration.

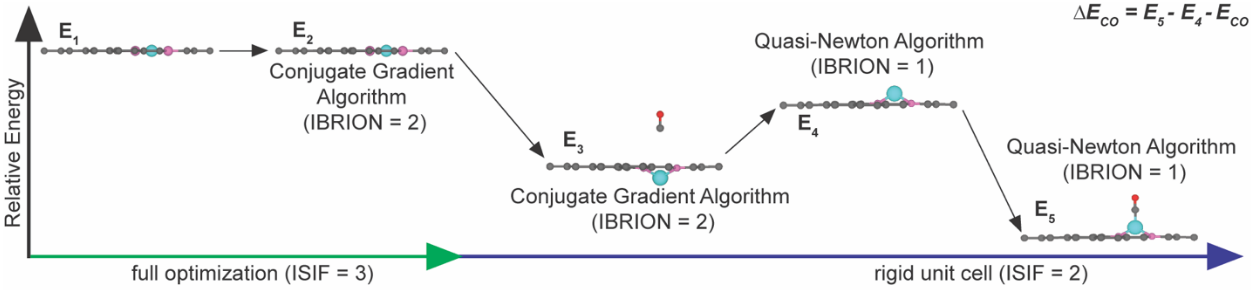

$\Delta E_{CO} = E_5 - E_4 - E_{CO}$
Relative Energy
E_1
E_2
Conjugate Gradient Algorithm (IBRION = 2)
E_3
Conjugate Gradient Algorithm (IBRION = 2)
Quasi-Newton Algorithm (IBRION = 1)
E_4
Quasi-Newton Algorithm (IBRION = 1)
E_5
full optimization (ISIF = 3)
rigid unit cell (ISIF = 2)

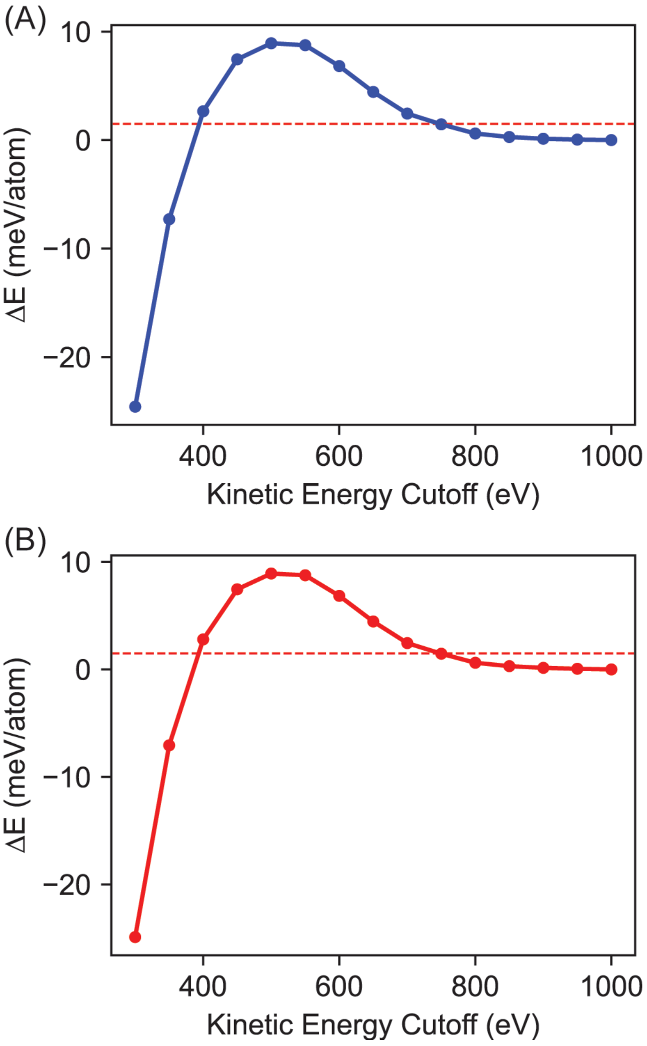

Figure S1. Energy differences per atom with respect to the energy of using a kinetic energy cutoff of 1000 eV in kinetic energy cutoff benchmark calculations for (A) Cu-N-C and (B) Zn-N-C SACs. The red dashed line indicates a value of 1.5 meV/atom. These calculations were performed using a Monkhorst-Pack *k*-point grid of 4×4×1.

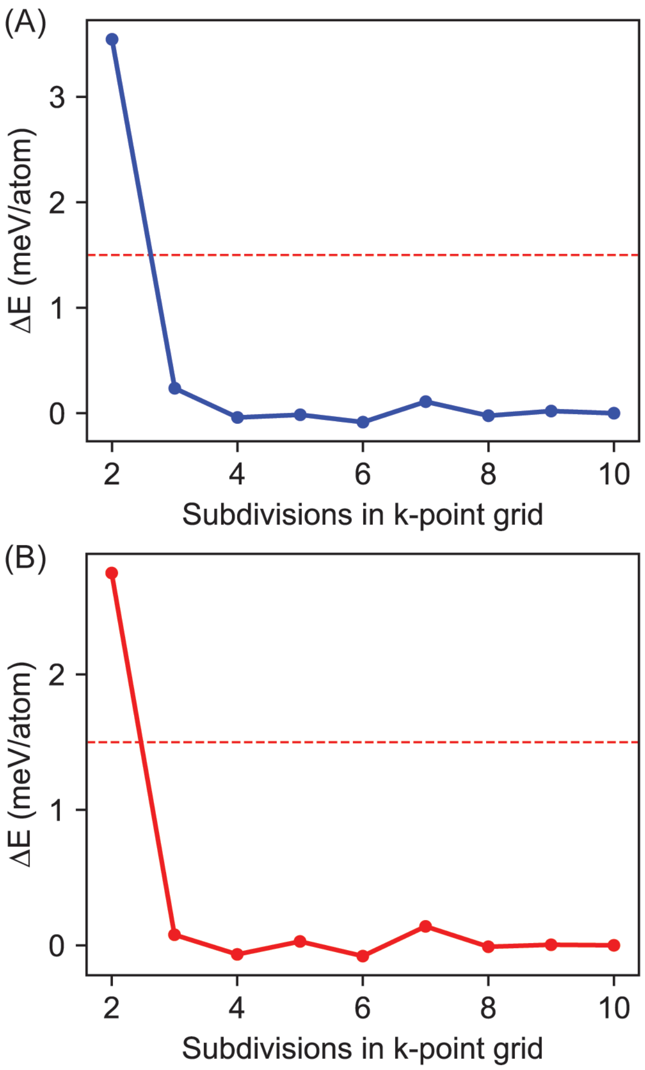

Figure S2. Energy differences per atom with respect to the energy of using a k-point grid of 10×10×1 in k-point grid benchmark calculations for (A) Cu-N-C and (B) Zn-N-C SACs. All calculations were performed using a kinetic energy cutoff of 800 eV. The red dashed line indicates a value of 1.5 meV/atom.

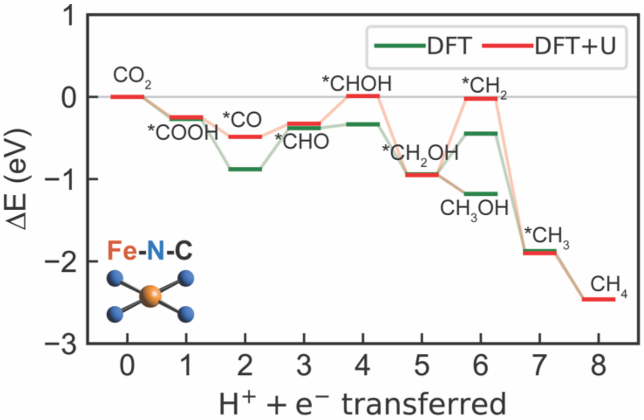

Figure S3. Energetics of CO2R to methane and methanol on Fe-N-C predicted by DFT calculations (green lines) and DFT+U calculations (red lines).

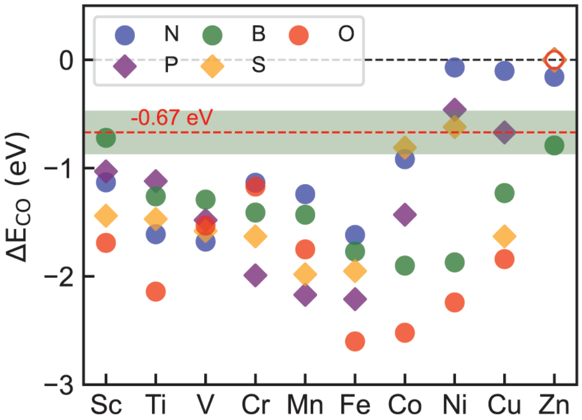

Figure S4. CO adsorption energies (ΔE_{CO}) of all *3d*-transition metals embedded on nitrogen- (blue spheres), boron- (green spheres), oxygen- (red spheres), phosphorus- (purple diamonds), and sulfur-doped (yellow diamonds) graphene. The red line indicates the optimal CO adsorption energy that predicts the most catalytically active catalysts for electrochemical CO_2R. A range of ± 0.2 eV from the optimal line is shown in the shaded green region to indicate the promising candidates. Empty symbols indicate unstable SACs.

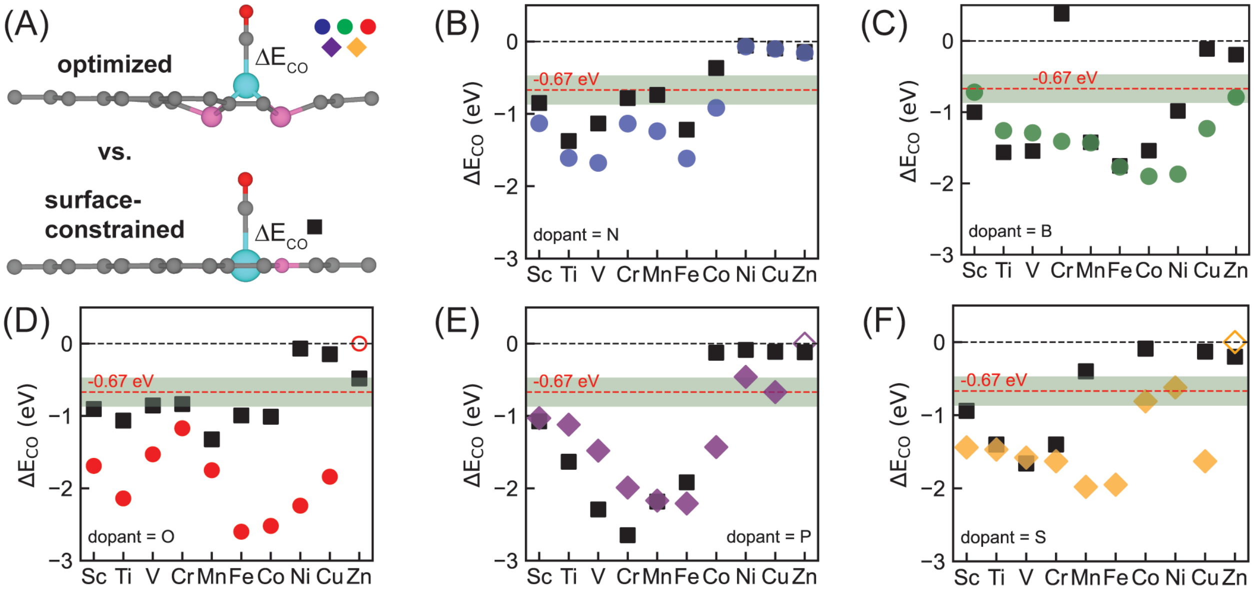

Figure S5. (A) Representative CO-adsorbed SAC structures in full geometry optimizations (top) and constrained geometry optimizations (bottom). Comparison of CO adsorption energies predicted by full and constrained geometry optimizations (black squares) for (B) nitrogen-doped, (C) boron-doped, (D) oxygen-doped, (E) phosphorus-doped, and (F) sulfur-doped SACs.

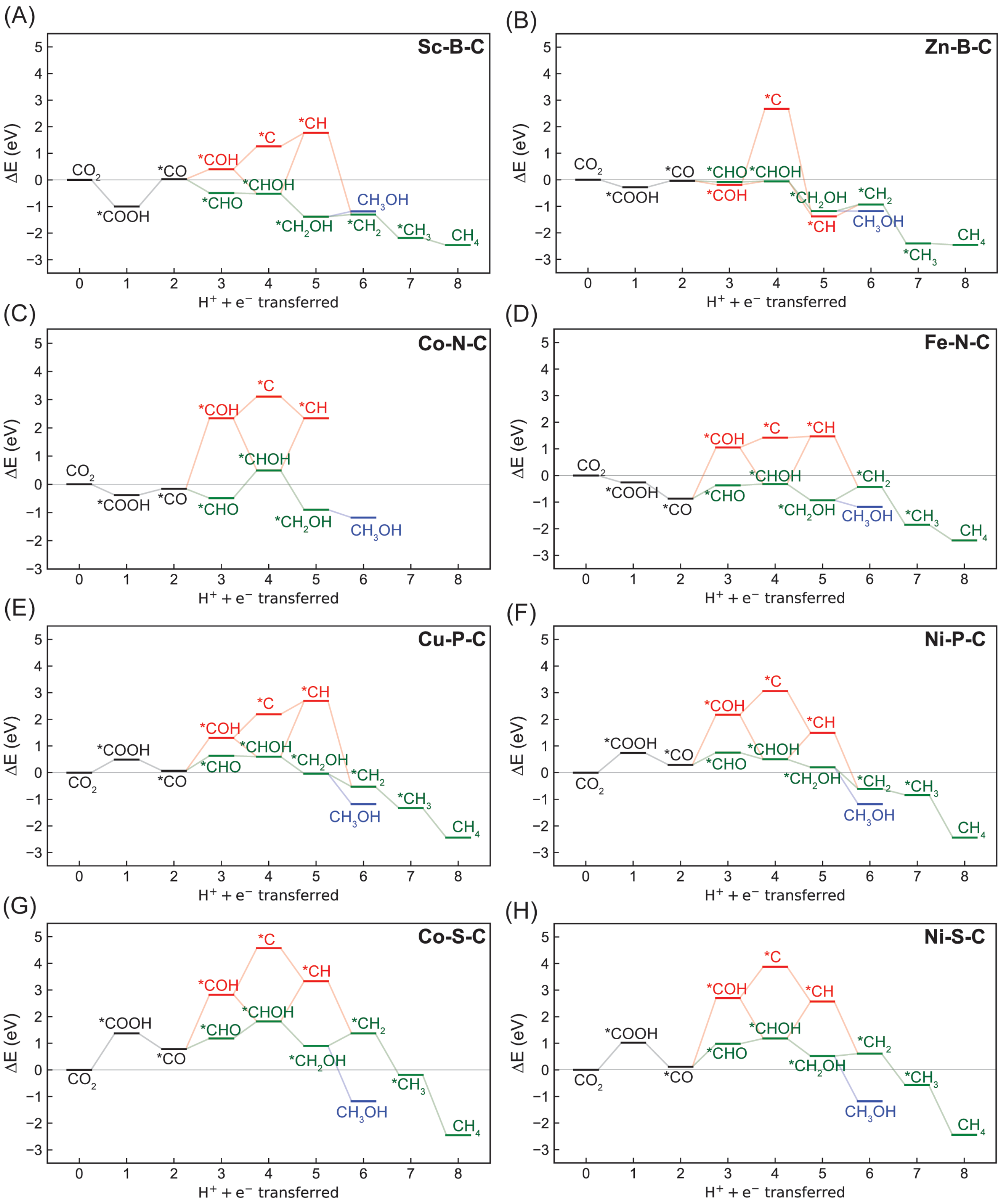

Figure S6. Energetics of all possible reaction pathways of CO₂R to methane via eight PCET steps and methanol via six PCET steps on (A) Sc-B-C, (B) Zn-B-C, (C) Co-N-C, (D) Fe-N-C, (E) Cu-P-C, (F) Ni-P-C, (G) Co-S-C, and (H) Ni-S-C predicted by DFT-PBE-D3. The green lines show the most favorable pathway toward methane or methanol formation through a *CHO intermediate identified on most SACs except for Zn-B-C. The red lines denote other possible pathways. Blue lines indicate formation of methanol.

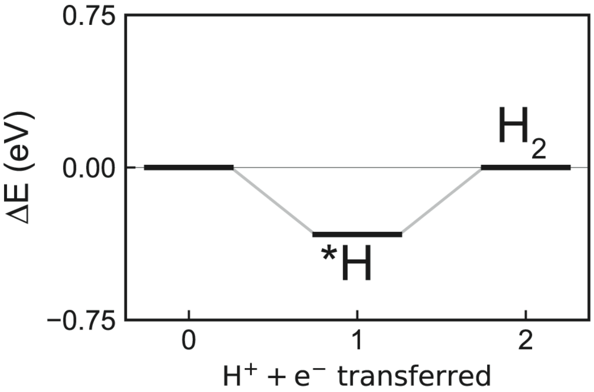

Figure S7. Energetics of HER on Zn-B-C predicted by DFT-PBE-D3.

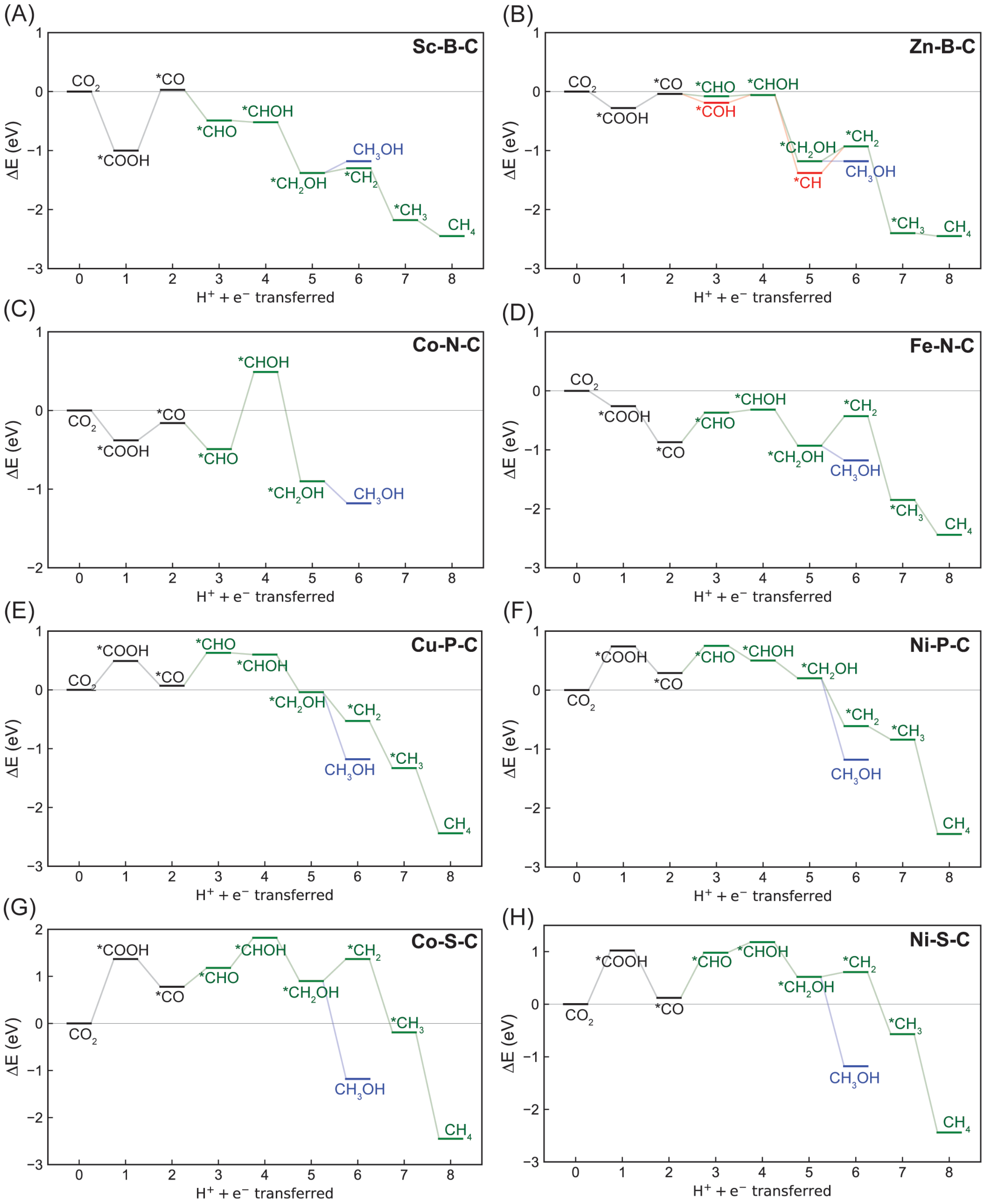

Figure S8. Energetics of the most favorable reaction pathways of CO_2R to methane via eight PCET steps and methanol via six PCET steps on (A) Sc-B-C, (B) Zn-B-C, (C) Co-N-C, (D) Fe-N-C, (E) Cu-P-C, (F) Ni-P-C, (G) Co-S-C, and (H) Ni-S-C predicted by DFT-PBE-D3. The green lines show the most favorable pathway toward methane or methanol formation through a *CHO intermediate identified on most SACs except for Zn-B-C. The red lines denote other favorable pathways on Zn-B-C. Blue lines indicate formation of methanol.

Table S1. Geometries of optimized SAC clean surfaces with metal centers varying from Sc, Ti, V, Cr, Mn, Fe, Co, Ni, Cu, to Zn, and dopants varying from N, B, O, P, to S.

	N	**B**	**O**	**P**	**S**
Sc	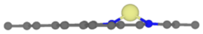	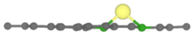	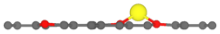	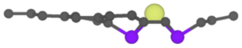	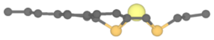
Ti				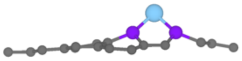	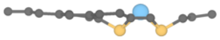
V	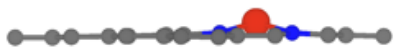			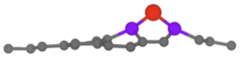	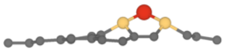
Cr			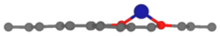	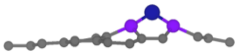	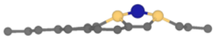
Mn			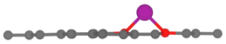	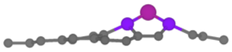	
Fe				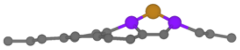	
Co				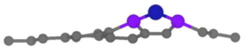	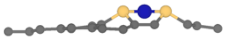
Ni					
Cu					
Zn				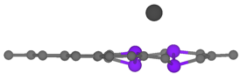	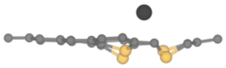

Table S2. Energy differences of nitrogen-doped SACs in eV between using different initial magnetic moments guesses and using the default initial magnetic moment guess of 1.

Initial magnetic moment	0	1	2	3	4	5	6
Sc-N-C	-	0.00	-	-	-	-	-
Ti-N-C	0.00	0.00	0.00	-	-	-	-
V-N-C	-	0.00	-	0.00	-	-	-
Cr-N-C	0.00	0.00	0.00	0.00	0.00	0.0	0.00
Mn-N-C	-	0.00	-	-0.01	-	-0.01	-
Fe -N-C	0.00	0.00	0.00	-	0.00	-	-
Co-N-C	-	0.00	-	0.00	-	-	-
Ni-N-C	0.00	0.00	0.00	-	-	-	-
Cu-N-C	0.00	0.00	-	-	-	-	-
Zn-N-C	0.00	0.00	-	-	-	-	-

Table S3. Final magnetic moments on nitrogen-doped SACs using different initial magnetic moment guesses.

Initial magnetic moment	0	1	2	3	4	5	6
Sc	-	0.007	-	-	-	-	-
Ti	1.694	1.694	1.695	-	-	-	-
V	-	2.929	-	2.929	-	-	-
Cr	4.015	4.015	4.015	4.016	4.015	4.015	4.015
Mn	-	3.001	-	3.001	-	3.001	-
Fe	1.992	1.991	1.992	-	1.992	-	-
Co	-	0.946	-	0.946	-	-	-
Ni	0.000	0.000	0.000	-	-	-	-
Cu	1.047	1.047	-	-	-	-	-
Zn	0.000	0.000	-	-	-	-	-

Table S4. Comparison of CO adsorption energies (ΔE_{CO}) in eV on nitrogen-doped SACs between without and with dipole energy and field correction.

	ΔE_{CO} (no dipole correction) (eV)	ΔE_{CO} (with dipole correction) (eV)
Sc-N-C	-1.131	-1.133
Ti-N-C	-1.610	-1.606
V-N-C	-1.678	-1.679
Cr-N-C	-1.135	-1.132
Mn-N-C	-1.240	-1.233
Fe-N-C	-1.617	-1.613
Co-N-C	-0.917	-0.915
Ni-N-C	-0.070	-0.070
Cu-N-C	-0.102	-0.102
Zn-N-C	-0.156	-0.155

Table S5. Complexation energy in eV of five representative SACs.

SAC	Fe-N-C	Sc-B-C	Ni-O-C	Cu-P-C	Co-S-C
$E_{complexation}$ (eV)	-8.41	-6.17	-2.43	-17.26	-22.79

Table S6. Representative geometries of three possible adsorption sites, i.e., atop, bridge, hollow, considered for key intermediates.

	atop	bridge	hollow
*COH	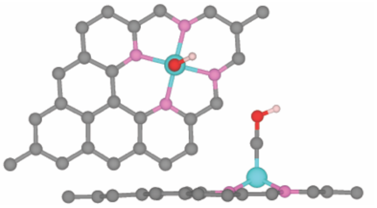	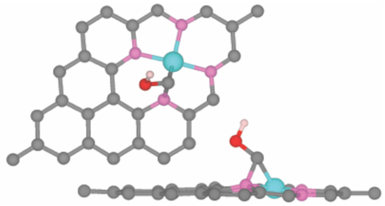	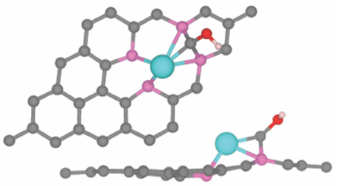
*C	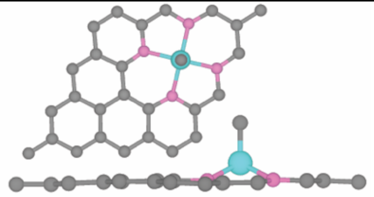	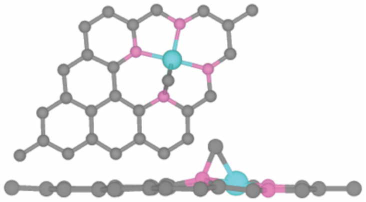	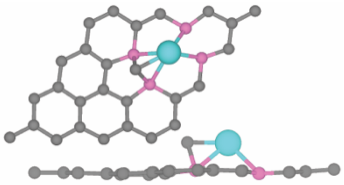
*CH	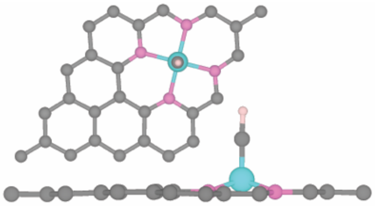	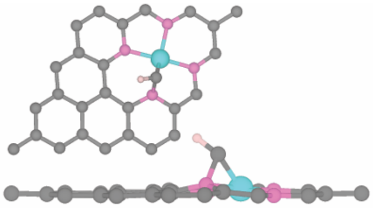	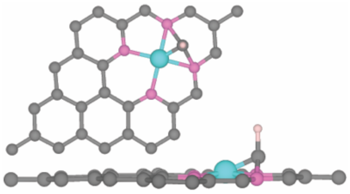
*CH_2	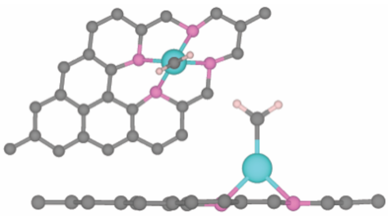	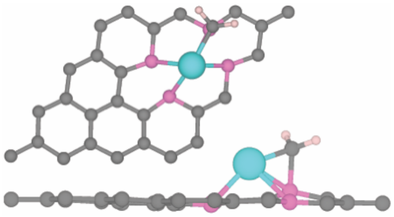	N/A
*CHOH	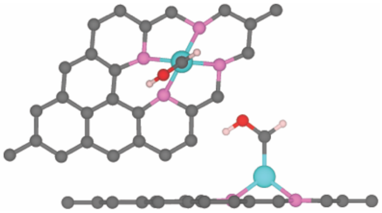	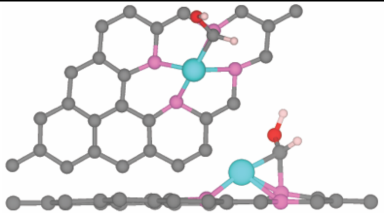	N/A

Table S7. Preferred adsorption site of key CO_2R intermediates on various SACs predicted by DFT-PBE-D3.

	Sc-B-C	Zn-B-C	Co-N-C	Fe-N-C	Ni-P-C	Cu-P-C	Co-S-C	Ni-S-C
*COH	hollow	hollow	atop	atop	bridge	hollow	atop	atop
*CHOH	bridge	bridge	atop	atop	bridge	bridge	atop	atop
*C	bridge	hollow	atop	atop	bridge	hollow	bridge	bridge
*CH	atop	hollow	atop	atop	bridge	atop	bridge	hollow
*CH_2	bridge	bridge	-	atop	bridge	bridge	bridge	bridge

Table S8. Reaction energies in eV for each considered step of electrochemical CO_2R to methane and methanol on Sc-B-C, Zn-B-C, Co-N-C, Fe-N-C, Ni-P-C, Cu-P-C, Co-S-C, and Ni-S-C predicted by DFT-PBE-D3. The corresponding reaction pathways are shown in Figure S5.

	Sc-B-C	Zn-B-C	Co-N-C	Fe-N-C	Ni-P-C	Cu-P-C	Co-S-C	Ni-S-C
$CO_2 + H^+ + e^- \rightarrow {}^*COOH$	-1.00	-0.28	-0.38	-0.26	0.74	0.49	1.37	1.02
${}^*COOH + H^+ + e^- \rightarrow {}^*CO + H_2O$	1.03	0.24	0.22	-0.61	-0.45	-0.42	-0.59	-0.90
${}^*CO + H^+ + e^- \rightarrow {}^*CHO$	-0.52	-0.04	-0.33	0.50	0.46	0.56	0.40	0.86
${}^*CO + H^+ + e^- \rightarrow {}^*COH$	0.37	-0.15	2.49	1.92	1.88	1.23	2.04	2.58
${}^*CHO + H^+ + e^- \rightarrow {}^*CHOH$	-0.03	0.02	0.98	0.05	-0.25	-0.03	0.64	0.20
${}^*COH + H^+ + e^- \rightarrow {}^*CHOH$	-0.92	0.13	-1.84	-1.37	-1.67	-0.70	-1.00	-1.52
${}^*COH + H^+ + e^- \rightarrow {}^*C + H_2O$	0.86	2.86	0.79	0.37	0.89	0.89	1.75	1.18
${}^*CHOH + H^+ + e^- \rightarrow {}^*CH_2OH$	-0.86	-1.12	-1.40	-0.61	-0.30	-0.64	-0.92	-0.66
${}^*CHOH + H^+ + e^- \rightarrow {}^*CH + H_2O$	2.29	-1.32	1.84	1.79	0.99	2.09	1.51	1.39
${}^*C + H^+ + e^- \rightarrow {}^*CH$	0.51	-4.05	-0.79	0.05	-1.57	0.50	-1.24	-1.31
${}^*CH_2OH + H^+ + e^- \rightarrow CH_3OH$	0.20	0.00	-0.27	-0.25	-1.38	-1.14	-2.08	-1.70
${}^*CH_2OH + H^+ + e^- \rightarrow {}^*CH_2 + H_2O$	0.08	0.25	-	0.50	-0.81	-0.49	0.47	0.09
${}^*CH + H^+ + e^- \rightarrow {}^*CH_2$	-3.07	0.45	-	-1.90	-2.10	-3.22	-1.96	-1.96

$*CH_2 + H^+ + e^-$ $\rightarrow *CH_3$	-0.88	-1.47	-	-1.42	-0.23	-0.80	-1.56	-1.18
$*CH_3 + H^+ + e^-$ $\rightarrow CH_4$	-0.26	-0.05	-0.52	-0.59	-1.60	-1.11	-2.25	-1.87